LiNi.Mn.O Cathode Materials Co-Doped with La^{3} and S^{2} for Use in Lithium-Ion Batteries

AUTHOR(S):

WANG, Wencong; HANZAWA, Hiromasa; MACHIDA, Ken-ichi; MIYAZAKI, Kohei; ABE, Takeshi

CITATION:

WANG, Wencong ...[et al]. LiNi.Mn.O Cathode Materials Co-Doped with La^{3} and S^{2} for Use in Lithium-Ion Batteries. Electrochemistry 2022, 90(1): 017010.

ISSUE DATE:

2022-01-15

URL:

http://hdl.handle.net/2433/277040

Electrochemistry
The Electrochemical Society of Japan
Received: November 17, 2021
Accepted: December 7, 2021
Published online: December 11, 2021
Issued: January 15, 2022
https://doi.org/10.5796/electrochemistry.21-00119
https://doi.org/10.50892/data.electrochemistry.17157863
Article
Electrochemistry, **90(1)**, 017010 (2022)

$LiNi_{0.5}Mn_{1.5}O_4$ Cathode Materials Co-Doped with La^{3+} and S^{2-} for Use in Lithium-Ion Batteries

Wencong WANG,[a,b] Hiromasa HANZAWA,[a] Ken-ichi MACHIDA,[a] Kohei MIYAZAKI,[b,*,§] and Takeshi ABE[b,§]

[a] *Graduate School of Engineering, Osaka University, 2-1 Yamadaoka, Suita, Osaka 565-0871, Japan*
[b] *Graduate School of Engineering, Kyoto University, Katsura, Nishikyo-ku, Kyoto 615-8510, Japan*

* *Corresponding author: myzkohei@elech.kuic.kyoto-u.ac.jp*

ABSTRACT

Spherical $LiNi_{0.5}Mn_{1.5}O_4$ particles co-doped with lanthanum (La) and sulfur (S) were synthesized by a facile co-precipitation assisted solid-state annealing method with stable oxysulfide La_2O_2S (x = 0, 0.3, 0.5, 0.7, 1.0, and 1.2 at%) as a dopant. The prepared composite materials exhibited a slight shrinkage of lattice parameters without any impurity phase under $x \leq 0.7$ at%, and the Ni/Mn disordered arrangement in the spinel lattice increased with an increase in the ratio of dopants, as confirmed by X-ray diffraction and Raman spectroscopy. X-ray photoelectron spectroscopy and electrochemical measurements also clearly indicated that the residual Mn^{3+} in the cubic lattice could be effectively eliminated with the use of La_2O_2S dopants. The composite materials showed outstanding rate and cycling performance compared with those of the pristine material. Specifically, the material doped with 0.5 at% La_2O_2S showed a high reversible capacity of 115.9 mAh g^{-1} at 10 C, and a remarkable cycling performance of 109.2 mAh g^{-1} even after 200 cycles. All of these extraordinary performances were attributed to the synergistic effects of La and S in the spinel structure, which induce a suitable pathway for lithium ion and a robust architecture during the electrochemical assessment.

Keywords : Li-rich Layered Cathodes, Doping, Li-ion Diffusion, High-rate Performance

1. Introduction

Under the dual pressures of energy demands and environmental pollution, traditional fossil fuels like oil and coal must be replaced with renewable energy sources. Since renewable energies such as solar, wind, and geothermal have diverse forms, the use of effective energy-storage devices is crucial for their widespread use.[1–3] Among multiple proposed solutions, lithium-ion batteries (LIBs) are gaining attention due to their high energy density, long-cycle stability, portability, and relatively low cost.[4–7] With the development of energy-consuming devices such as mobile phones and electric vehicles, LIBs with higher energy density are required. As an important part of LIBs, cathode materials with a high working potential and discharge capacity are needed to effectively enhance the energy density of LIBs.[8–10]

Spinel-type $LiNi_{0.5}Mn_{1.5}O_4$ (LNMO) has received considerable attention as an inexpensive and abundant raw material. In addition, LNMO shows a high working potential of about 4.7 V (vs. Li^+/Li), a high theoretical capacity of 147 mAh g^{-1},[11] and a relatively high energy density (650 Wh kg^{-1}) compared with currently used materials such as layer-type $LiCoO_2$ (540 Wh kg^{-1}),[12] or olive-type $LiFePO_4$ (500 Wh kg^{-1}).[13] However, there are still some challenges for the application of LNMO materials. First, due to their low electronic and ionic conductivity, lithium ions tend to gather at the surface of the electrode, which causes over-lithiation at the surface of the electrode, resulting in the decomposition of surface particles and the formation of a distorted spinel phase of $Li_{1+\delta}Ni_{0.5}Mn_{1.5}O_4$.[14,15] Second, the conventional solid-state method for the synthesis of LNMO materials without sufficient mixing of the precursor usually introduces impurity phases such as $Li_xNi_{1-x}O$, which is unfavorable for the cycling performance of LNMO materials in LIBs. Third, in the calcination process, the LNMO phase usually decomposes into two different phases. One of these phases shows the $P4_332$ space group with an ordered arrangement of Ni^{2+}, Mn^{4+}, and Li^+ in the spinel structure, and the other phase belongs to the $Fd\bar{3}m$ space group with a disordered arrangement of randomly located Ni^{2+} or Mn^{4+} at transition sites due to the oxygen vacancy.[16–18] Many researchers have reported that LNMO materials with a disordered structure show enhanced electrochemical performance due to their relatively high ion conductivity. Furthermore, the transition of Mn^{4+} to Mn^{3+} ions to compensate for the loss of oxygen in the disordered phase would produce an undesirable Jahn-Teller effect during electrochemical measurements.[19–21] To address these challenges, the use of dopants such as Ru,[14] Cr,[17] Cu,[22] Zn,[23] Ti,[24] and Al,[25] for cations, as well as P,[26] S,[27] and F,[28] for anions has been proposed. With an optimized crystal structure and surface stability, cation- and anion-doped materials can impede corrosion due to hydrogen fluoride (HF) formed from the decomposition of the electrolyte, especially at a high potential and temperature.

Lanthanide rare earth elements such as Nd,[29] Er,[30] Sm,[31] and Ce[32] have been applied in many fields such as fluorescence, magnetism, and LIBs due to their special 4f orbital effects. Substituting partial Mn sites with La^{3+} to mitigate the leaching effect of Mn^{3+} in $LiMn_2O_4$ by sol-gel method has been reported to give excellent rate capability and cycling performance.[33]

In this study, we prepared a mixed cation-anion type of $LiNi_{0.5}Mn_{1.5-x}La_xO_{4-\delta}S_\delta$ (LNMO-x%La_2O_2S) spinel compounds with a simple solid-state method assisted with the co-precipitation process. As a result, the composite material doped with 1 % La and 0.5 % S exhibited excellent Li^+ storage performance, achieving a reversible capacity of about 115 mAh g^{-1} for 200 cycles at a high rate of 10 C.

§ECSJ Active Member
K. Miyazaki orcid.org/0000-0001-5177-3570
T. Abe orcid.org/0000-0002-1515-8340

2. Experimental

2.1 Material preparation and characterization

The pristine spinel LNMO and La_2O_2S-doped LNMO with different atomic ratios were synthesized by a typical co-precipitation method followed by stepwise calcination. $NiSO_4{\cdot}6H_2O$ (99.9 %, Wako Pure Chemical) and $MnSO_4{\cdot}H_2O$ (97 %, Alfa Aesar) were dissolved in deionized water to form a uniform aqueous solution under rapid stirring. A certain amount of 2 mol dm^{-3} (M) $(NH_4)_2CO_3$ (Wako Pure Chemical) as a precipitating and complexing agent was dropped into a reaction vessel so that the final pH of the solution would remain at 7.7, as determined by a pH controller (D-220P, Horiba Co.). To compensate for a few by-products of $Ni(NH_3)_6^{2+}$ (soluble) during synthesis,[34,35] the ratio of Ni : Mn was fixed at 1 : 2. After the mixture was stirred at room temperature for 30 min, a suspended solution was transferred to an autoclave at 55 °C for 3 h to cultivate uniform particles. The precursor was then collected by vacuum filtration and washed several times with distilled water. A vacuum dehydration process was conducted at 70 °C for 12 h. To make up for the vaporized lithium during hyperthermal crystallization, a slight excess (about 2 %) of lithium carbonate (Li_2CO_3, Wako Pure Chemical) was mixed with the precursor by a ball-milling method and finally pressed into a pellet at a pressure of 5 MPa. A series of dual-doped materials were prepared by the same process with stoichiometric La_2O_2S as the dopant. La_2O_2S was synthesized by a conventional flux method using Na_2CO_3 (Wako Pure Chemical) and S powder (Wako Pure Chemical) as a mixed flux to react with La_2O_3 (Wako Pure Chemical) under argon gas. Additional details of the pure La_2O_2S powder can be found in the literature.[36,37] To the best of our knowledge, due to the high reactivity of sulfur powder with oxygen under elevated temperature, it is difficult to use this material for S-doping under an air atmosphere. La_2O_2S is a lanthanide oxysulfide with high thermal stability and chemical stability. Therefore, sulfur can be stabilized in La_2O_2S before entering into the spinel lattice of LNMO. Heat treatment of the LNMO material was conducted at 500 °C for 5 h to form metal oxide. This was followed by sintering at 875 °C for 12 h to crystallize at a heating rate of 5 °C/min and the product was left to cool in the air.

The crystal structure of the synthesized powders was analyzed by powder X-ray diffraction (XRD, RIGAKU-RINT2200) with a monochromatic CuKα source at 40 kV, 30 mA. The XRD pattern was collected within an angle range of 15–80°, with a step size of 0.02°/3 s. Changes in the lattice parameters and the unit cell volume were calculated by Rietveld refinement using the GSAS program. Scanning electron microscopy (SEM, HITACHI-S-3000) was used to observe the surface morphologies of the samples. Energy dispersive X-ray spectroscopy (EDX, HORIBA-7021-H) and an electron probe micro-analyzer (EPMA, JXA-8800R, JEOL Ltd.) were used to analyze the element ratios in the LNMO electrode co-doped with La_2O_2S. Raman spectra (Thermo DXR FT-Raman spectrometer) were obtained with a single 532 nm laser pulse, and X-ray photoelectron spectrometry (XPS, Shimadzu Corp., Kratos AXIS-165x) with an AlKα source was performed to study the compositions and the crystal characteristics of the samples.

2.2 Electrochemical measurements and analyses

An assembly-type half-cell (Hohsen Corp.) with lithium metal foil as a counter electrode and a Celgard 2500 membrane as a separator was used to evaluate the electrochemical performance. A slurry composed of active materials, conductive acetylene black and polyvinylidene difluoride (PVdF) binder, in a mass ratio of 8 : 1 : 1 with a suitable amount of *N*-methyl-2-pyrrolidone (NMP) as a solvent was used to prepare the working electrode. The well-blended slurry was spread on the aluminum foil and dried at 120 °C for 12 h under vacuum to fabricate the cathode electrode. 1 M $LiPF_6$ dissolved in ethylene carbonate (EC) and diethyl carbonate (DEC) in a volume ratio of 1 : 1 (Kishida Chemical Co. Ltd.) was used as the electrolyte. To assemble a half-cell, a glove box filled with highly purified Ar gas ($O_2 \leq 1$ ppm; $H_2O \leq 1$ ppm) was used to reduce the environmental impact. The charge-discharge performance test and cyclic voltammetry (CV) were conducted with a battery tester (KIKUSUI, PFX2011) and automatic polarization system (HOKUTO DENNKO), respectively, in a potential range of 3.6–5.0 V (vs. Li^+/Li) at room temperature. AC impedance spectroscopy measurements (HIOKI 3532-80) were carried out with an AC amplitude voltage of 5 mV and the frequency range was set between 100 kHz–4 Hz.

3. Results and Discussion

Powder XRD measurements were conducted to confirm the crystal structure of the LNMO composite materials with various molar ratios of La_2O_2S as a dopant, as shown in Fig. 1. All of the diffraction patterns can be indexed as a well-crystallized cubic spinel structure. When the molar ratio of the La_2O_2S dopant was below 0.7 %, peaks representing an impurity rock salt phase (such as $Li_xNi_{1-x}O$ and Ni_xO as mentioned above) and lanthanide compounds could not be observed, illustrating that the co-precipitation method with a carbonate precursor was effective for providing atomic-level mixing and small amounts of La and S could be successfully introduced into the matrix structure of the LNMO

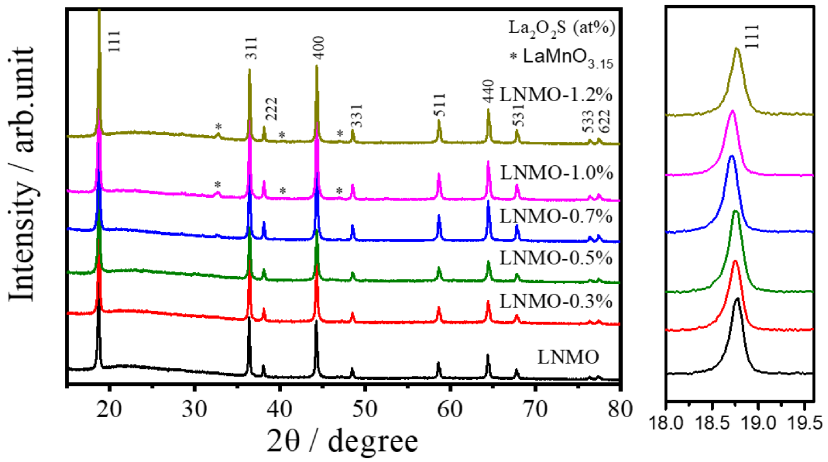

Figure 1. XRD patterns for LNMO-*x*%La_2O_2S (x = 0, 0.3, 0.5, 0.7, 1.0, and 1.2) and magnified XRD patterns of 111 plane. Impurity phase of $LaMnO_{3.15}$ is noted as (*).

Table 1. Lattice parameters (a), volumes (V), R factors (R_p and R_{wp}), and I_{311}/I_{400} values for LNMO-x%La_2O_2S ($x = 0$, 0.3, 0.5, 0.7, 1.0, and 1.2).

Sample	a (Å)	V (A^3)	R_p (%)	R_{wp} (%)	I_{311}/I_{400}
LNMO	8.1679	544.98	3.37	4.64	1.014
LNMO-0.3 %La_2O_2S	8.1671	544.76	4.46	3.31	1.032
LNMO-0.5 %La_2O_2S	8.1652	544.38	4.42	3.33	1.046
LNMO-0.7 %La_2O_2S	8.1645	544.23	3.56	4.83	0.998
LNMO-1.0 %La_2O_2S	8.1621	543.76	4.68	6.77	0.992
LNMO-1.2 %La_2O_2S	8.1607	543.48	3.91	5.47	0.981

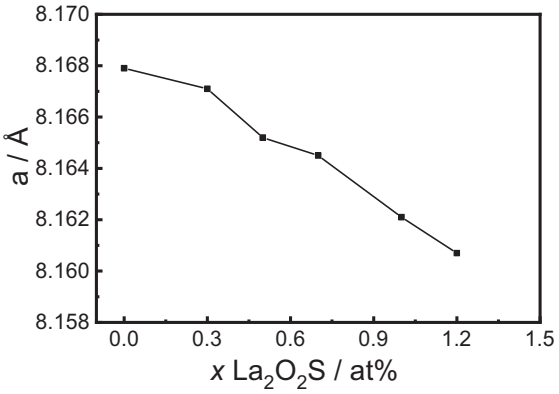

Figure 2. Lattice parameters calculated from XRD patterns as a function of La_2O_2S ratio in LNMO-x%La_2O_2S ($x = 0$, 0.3, 0.5, 0.7, 1.0, and 1.2).

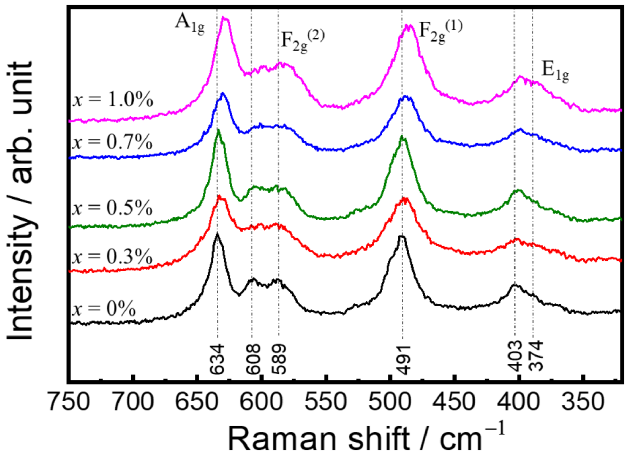

Figure 3. Raman spectra of LNMO-x%La_2O_2S ($x = 0$, 0.3, 0.5, 0.7, and 1.0).

materials. However, with an increase in the ratio of La_2O_2S, the existence of the impurity orthorhombic phase $LaMnO_{3.15}$ (ICDD #89-0680) at 32.6, 40.1, and 46.8° was confirmed, and is noted by the symbol (*) in the pattern. A magnified image of the peaks of 111 diffractions is shown in Fig. 1. With the addition of the dual-elements, the diffraction peaks shifted to higher angles.

The changes in the lattice parameter (a) and the unit cell volume were calculated by the Rietveld refinement, and the results are summarized in Table 1 and Fig. 2. The parameter decreased slightly from 8.167(9) to 8.160(7) Å with an increase in the ratio of the doping elements. This change seems a little odd since the cation radius of La^{3+} (1.03 Å) is larger than those of Mn^{4+} (0.53 Å) and Mn^{3+} (0.645 Å) and the anion radius of S^{2-} (1.70 Å) is also larger than that of O^{2-} (1.26 Å).[27] There are several possible explanations for the abnormal shrinkage. First, the binding energy of La–O (798 kJ mol^{-1}, 298 K) is more than twice that of the Mn–O (358.2 kJ mol^{-1}, 298 K), even with the addition of a very small amount of heteroatoms, resulting in a stronger shrinkage effect in the spinel crystal lattice.[38] This phenomenon can also be found in materials modified with other rare earth elements, such as Sm- or Tb-doped LNMO from previous studies.[31,39] Second, due to the introduction of La^{3+} to replace Mn^{3+}/Mn^{4+}, the residual Mn^{3+} in the cubic lattice tended to be oxidized into Mn^{4+}. As a result, a higher ratio of Mn^{4+} with a smaller ionic radius could decrease the lattice parameters to some extent.[31] Meanwhile, the oxygen vacancy sites were partly occupied by anion S^{2-} during calcination to maintain the charge neutrality, which facilitated the conversion of Mn^{3+}/Mn^{4+} as mentioned above.

To further reveal the difference in structural stability among the samples, the ratios of I_{311}/I_{400} (I refers to the intensity of the peaks in the XRD pattern) were calculated and the results are listed in Table 1. Previous studies have shown that when the value of the ratio is between 0.96 and 1.1, the samples may have a relatively robust spinel structure and show enhanced electrochemical performance.[38,40,41] All of the samples we prepared are within this range, and among them LNMO-0.5 %La_2O_2S showed the largest ratio, which suggests that La_2O_2S-doped materials have the potential to demonstrate improved electrochemical properties.

As discussed above, LNMO materials have two types of structure that is determined by the Ni/Mn arrangement in the octahedral sites of the spinel structure. To further distinguish these similar architectures, Raman spectroscopy was used to examine the crystal properties of LNMO as shown in Fig. 3. The scattering bands at 400 and 490 cm^{-1} could be attributed to the E_{1g} and $F_{2g}^{(1)}$ stretching vibration modes of Ni^{2+}–O. The peaks at around 588–610 and 630 cm^{-1} were signatures of the $F_{2g}^{(2)}$ symmetrical stretching vibration mode of Mn^{4+}–O group and the A_{1g} symmetric stretching vibration mode [MnO_6], respectively.[42] For the pristine LNMO, a pair of splitting peaks attributed to $F_{2g}^{(2)}$ vibration were observed, indicating that the major phase of the LNMO sample tended to form an ordered structure with a $P4_332$ space group rather than the disordered structure of $Fd\bar{3}m$. Compared with pristine LNMO, the $F_{2g}^{(2)}$ band in the La_2O_2S-doped LNMO became ambiguous and a red-shift appeared with an increase in the doping ratio of La_2O_2S, suggesting that La and S intruded into the spinel structure and could increase the chaos in the transition metal sites.

Figure 4 compares the XPS spectra of the Mn2p orbital for the pristine LNMO and La_2O_2S-doped LNMO materials. From the fitting result of this high-resolution spectra, typical core-level spectra of $Mn2p_{3/2}$ and $Mn2p_{1/2}$ in the pristine LNMO material were confirmed at 642.3 and 654.2 eV. For those La_2O_2S-doped LNMO materials, however, the characteristic peaks of Mn2p shifted to 642.5 and 654.3 eV, respectively. It is widely known that the position of Mn^{4+} in the peak of $Mn2p_{3/2}$ occupies a higher energy level than Mn^{3+}, therefore the shift of Mn2p can be attributed to the

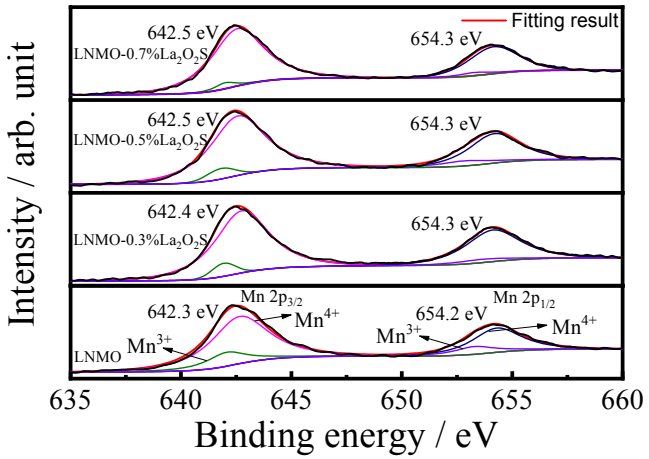

Figure 4. XPS spectra of Mn2p core-level for LNMO-x%La_2O_2S ($x = 0$, 0.3, 0.5, and 0.7).

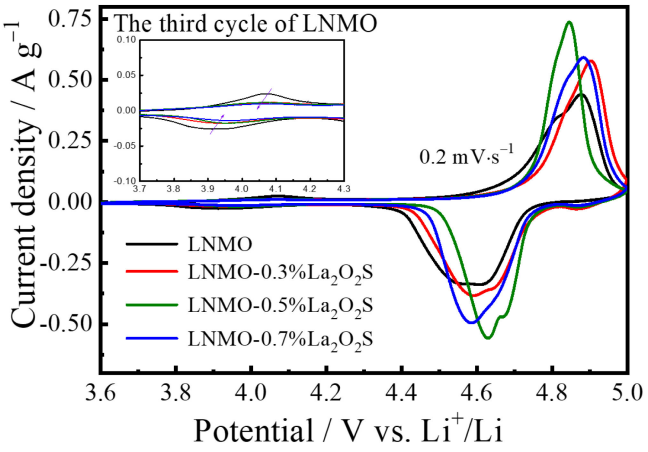

Figure 6. CV curves of LNMO-x%La_2O_2S ($x = 0$, 0.3, 0.5, and 0.7) at a scan rate of 0.2 mV s^{-1}. Inset figure is a magnified image at around 4 V.

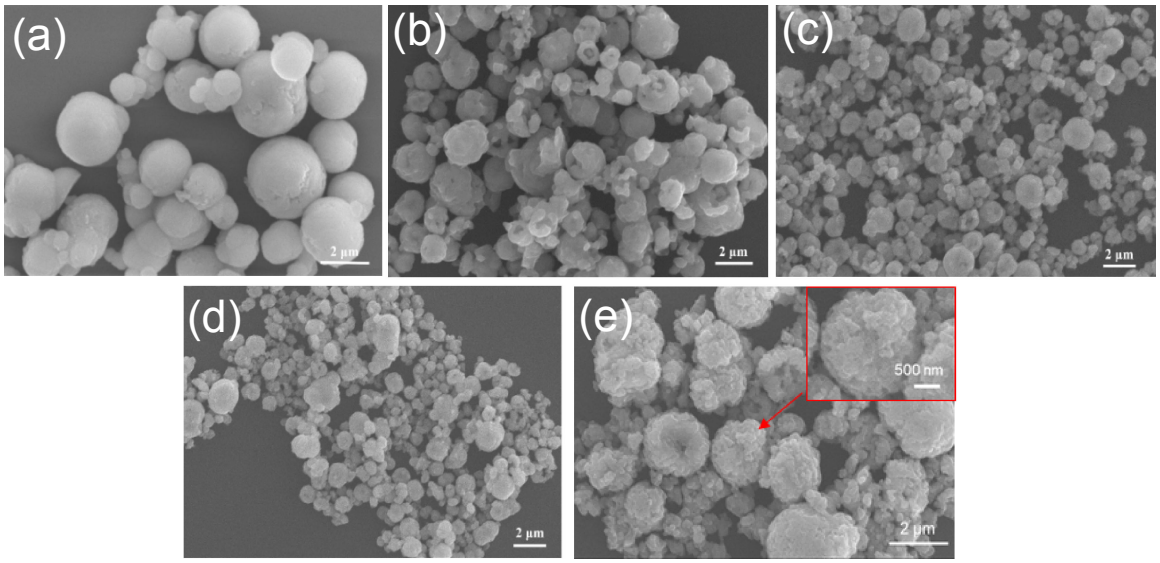

Figure 5. SEM images of (a) $Ni_{0.25}Mn_{0.75}CO_3$ precursor and (b–e) LNMO-x%La_2O_2S ($x = 0$, 0.3, 0.5, and 0.7).

change in the average chemical valence of Mn upon doping with La_2O_2S.[17,31,35] According to the fitting results of $Mn2p_{3/2}$, the ratio of Mn^{3+} of pristine LNMO was 18.1 %, and the ratio was greatly suppressed to 7.2 % in LNMO-0.5 %La_2O_2S. These results suggest that La_2O_2S dopants can decrease the ratio of Mn^{3+} in the LNMO spinel structure, which is consistent with the results of the Rietveld refinement analysis as mentioned above.

The changes in morphology during the doping process with La_2O_2S were revealed by SEM. As shown in Fig. 5a, the formation of a well-developed spherical precursor of $Ni_{0.25}Mn_{0.75}CO_3$ via a co-precipitation method was observed. Due to the lack of stability, the pristine LNMO showed some structural collapse after crystallization (Fig. 5b). However, for the 0.3 % La_2O_2S- and 0.5 % La_2O_2S-doped LNMO materials, secondary particles with a smooth surface and uniform size were observed (Figs. 5c–5d). When the ratio of La_2O_2S increased to 0.7 % (Fig. 5e), numerous tiny particles newly formed on the surface of the spherical particles, which made the surface rough and it was difficult for the particles to maintain their spherical structure. As shown in Figs. S1 and S2, the chemical composition of LNMO-0.5 %La_2O_2S composite material was further confirmed by the EDX and EPMA method, and the semi-quantitative results regarding the element ratio are summarized in Tables S1 and S2. Similar results were confirmed by both methods, coinciding with the stoichiometric proportion of each element.

To confirm the Li storage performance of the LNMO-x%La_2O_2S ($x = 0$, 0.3, 0.5, and 0.7) materials, a series of electrochemical measurements were carried out. Figure 6 shows the CV performance of the LNMO-x%La_2O_2S materials at a scan rate of 0.2 mV s^{-1}. The peaks at about 4.8 V were attributed to the stepwise redox reaction from Ni^{2+} to Ni^{4+}. According to the curves, LNMO-0.5 %La_2O_2S showed the most satisfactory electrochemical performance with the smallest polarization and excellent lithium-ion storage reactivity. Interestingly, as shown in the inset in Fig. 6, although the redox peaks at 4 V attributed to the Mn^{3+}/Mn^{4+} reaction during electrochemical cycling can still be confirmed under doping with different atomic ratios of La_2O_2S, the intensities of these redox peaks were significantly decreased compared with those of pristine LNMO. These results suggest that a small amount of La and S in the spinel lattice can effectively suppress the formation of Mn^{3+} and side reactions at the interface between the electrode and electrolyte.

Galvanostatic measurements were carried out to evaluate the electrochemical performance of LNMO-x%La_2O_2S. The rate capability of LNMO-x%La_2O_2S ($x = 0$, 0.3, 0.5, and 0.7) as working electrodes was compared within a current range of 0.5–

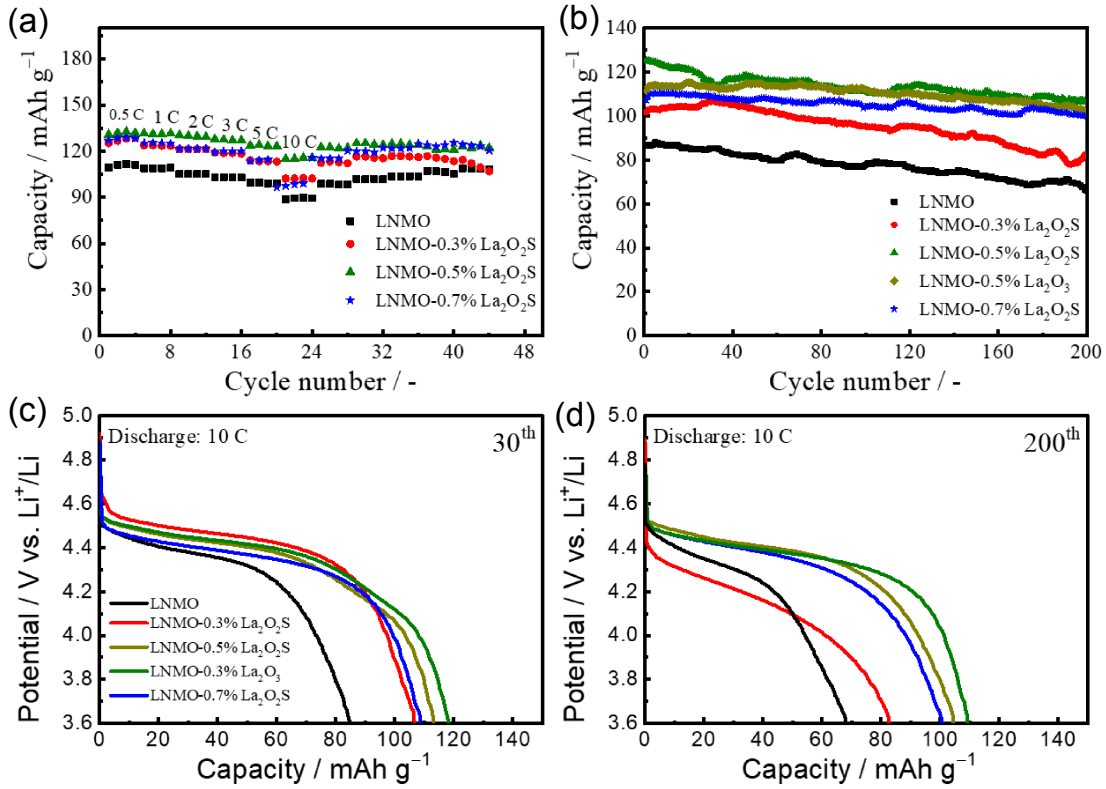

Figure 7. Rate and cycle performances of LNMO-x%La_2O_2S ($x = 0$, 0.3, 0.5, and 0.7), and LNMO-0.5 %La_2O_3. (a) Rate performance; (b) cycle performance under the condition of 1 C charge and 10 C discharge; discharge curves at (c) 30th and (d) 200th cycle.

10 C, as shown in Fig. 7a, which only shows the discharge capability. When the current was greater than 1 C, the charge current was fixed at 1 C and only the discharge current was changed for each rate.

LNMO-0.5 %La_2O_2S clearly showed the highest rate capabilities of 131.9, 132, 129.7, 127.4, 123.3, and 115.9 mAh g^{-1} at 0.5, 1, 2, 3, 5, and 10 C, respectively. For the pristine sample, however, these values were only 111.7, 108.9, 105.3, 103.2, 99.6, and 89.8 mAh g^{-1} under each rate. The capacity retention from 0.5 C to 10 C for the pristine LNMO electrode (80.4 %) was smaller than that for a LNMO-0.5 %La_2O_2S (87.9 %) composite electrode. All of the La_2O_2S-doped LNMO materials showed enhanced rate performance in contrast with that of the pristine LNMO electrode. Figure 7b compares the cycling durability for a discharge current of 10 C and a charge current of 1 C. The LNMO-0.5 %La_2O_2S composite electrode showed the highest reversible capacity of about 109.2 mAh g^{-1} after 200 cycles, which is lower than the value obtained in the rate-capability measurements. This difference might be due to material fatigue during the prolonged measurement under a high current density. However, the pristine LNMO electrode gave an inferior performance of only 67 mAh g^{-1} after 200 cycles with the same charge and discharge conditions. This suggests that the rate performance and structural stability of the LNMO electrode can be improved by doping with an appropriate ratio of La_2O_2S dopant. To understand the synergistic effects of La^{3+} and S^{2-} doped in LNMO, LNMO-0.5 %La_2O_3 was prepared by doping the LNMO material with only La_2O_3 to investigate the role of S anion. Interestingly, the electrode of LNMO-0.5 %La_2O_2S showed a slightly higher reversible capacity after 200 cycles at 10 C than that of the LNMO-0.5 %La_2O_3 composite electrode, indicating that the S anion in the spinel structure of LNMO might be able to promote Li^+ mobility and reinforce the structure of the electrode under a high current density. The discharge curves of LNMO-x%La_2O_2S and LNMO-0.5 %La_2O_3 composite electrodes after the 30th and 200th cycles under a current density of 10 C are shown in Figs. 7c and 7d, respectively. Due to the polarization effect and the poor conductivity under a high current density, the pristine LNMO electrode showed a short plateau below 4.4 V corresponding to the reduction reaction of Ni^{4+}. However, the La_2O_2S-doped LNMO electrodes gave a plateau at 4.5 V and had a better reversible capacity than the pristine LNMO electrode. The LNMO-x%La_2O_2S composite electrodes showed similar discharge curves at the 30th cycle. However, after the 200th cycle, the LNMO-0.3 %La_2O_2S electrode showed the worst capacity fading with a decrease in average potential, and its reversible capacity was almost equal to that of the pristine LNMO electrode. Therefore, the insufficient molar ratio of La_2O_2S dopant could not effectively mitigate the structural instability of LNMO during the long-term charge-discharge cycles, and the appropriate molar ratio of about 0.5 % La_2O_2S dopant is essential for improving its cycling performance. In addition, compared with the LNMO-0.5 %La_2O_3 composite electrode, the LNMO-0.5 %La_2O_2S electrode showed better cycling performance with a more durable capacity retention, which was attributed to the improvements in Li^+ mobility and the structural stability of the LNMO material corresponding to the synergistic effects of the (La, S) dual-elements.

Figure 8 compares the surface morphologies of pristine LNMO and LNMO-0.5 %La_2O_2S electrodes after the 200th cycle. Due to the poor structural stability of the pristine LNMO electrode, many cracks and residual products during the reversible lithium storage process were observed on the surface. However, the results were quite different for the LNMO-0.5 %La_2O_2S composite electrode, which had a relatively flat surface with regular particles that can be maintained during the prolonged electrochemical measurements. To discuss the roles of La and S in the composite electrodes, the apparent lithium-ion diffusion coefficient (D_{Li^+}) under different electrochemical processes was calculated with the following Randles-Sevick equation,[43] and the results are summarized in Table 2:

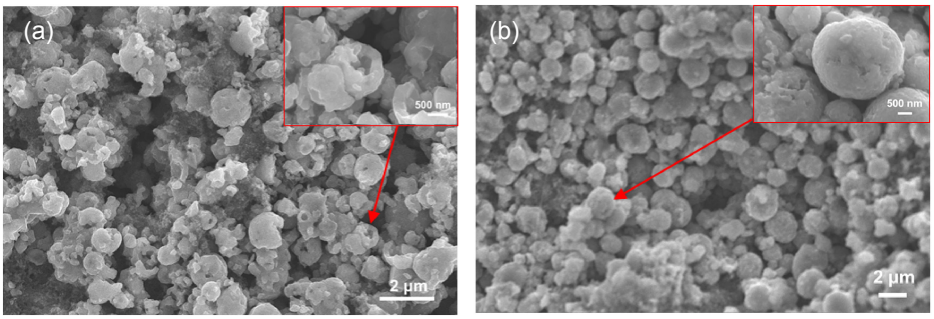

Figure 8. SEM images of (a) pristine LNMO and (b) LNMO-0.5 %La_2O_2S after the 200th cycle.

Table 2. Lithium diffusion coefficients (D_{Li^+}, cm^2/s) evaluated for pristine LNMO, LNMO-0.5 %La_2O_3, and LNMO-0.5 %La_2O_2S.

Samples	$Ni^{2+} \rightarrow Ni^{3+}$	$Ni^{3+} \rightarrow Ni^{4+}$	$Ni^{4+} \rightarrow Ni^{3+}$	$Ni^{3+} \rightarrow Ni^{2+}$
LNMO	5.01×10^{-11}	3.76×10^{-10}	3.55×10^{-10}	6.40×10^{-11}
LNMO-0.5 %La_2O_3	2.16×10^{-10}	1.49×10^{-9}	6.55×10^{-10}	2.86×10^{-10}
LNMO-0.5 %La_2O_2S	5.43×10^{-10}	3.39×10^{-9}	1.11×10^{-9}	4.62×10^{-10}

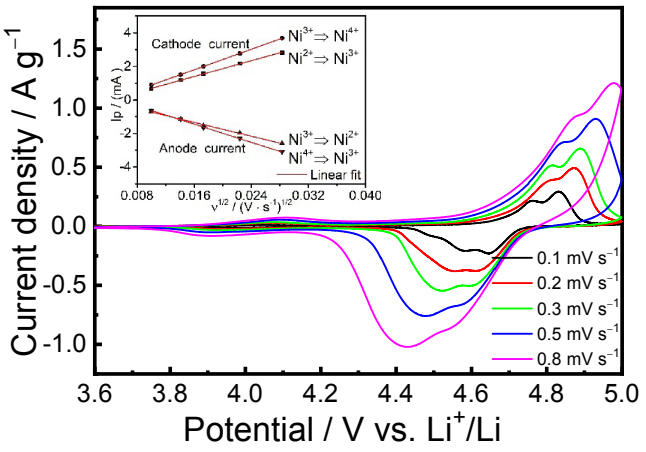

Figure 9. Kinetic analysis of pristine LNMO electrode by CV measurements at different scan rates. The inset image displays the liner fitting results between the peak currents and square root of the scan rates.

$$I_p = 2.69 \times 10^5 n^{3/2} A D_{Li^+}^{1/2} C_{Li^+} \upsilon^{1/2}$$

where n is the number of transferred electrons ($n = 1$, Li^+), A is the electrode area (1.13 cm^2), and C_{Li^+} is the concentration of Li^+ in the electrode (assuming that the oxidation reactions from Ni^{2+} to Ni^{3+} and Ni^{3+} to Ni^{4+} contribute half of the electron transfer number, 2.38×10^{-2} and 1.19×10^{-2} mol cm^{-3}, respectively).[44,45] Peak currents (I_p) during CV with different scan rates are shown in Fig. 9. From the inset, a well-fitted linear relationship between I_p and the square root of the scan rate ($\upsilon^{1/2}$) was confirmed. The values of D_{Li^+} for the LNMO-0.5 %La_2O_2S composite electrode were 3–10 times greater than that of the pristine LNMO during the charge and discharge stages. Interestingly, the different values of D_{Li^+} between the LNMO-0.5 %La_2O_3 and the LNMO-0.5La_2O_2S composite electrodes was ascribed to the synergistic effect of the (La, S) dual-elements. We inferred that a small amount of La^{3+} in the LNMO-0.5La_2O_2S composite electrode occupies transition metal sites in the structure of LNMO, and forms a robust bond with O that can stabilize the structure and inhibit the adverse effect of manganese. In addition, doping of S^{2-} would occupy some of the O sites in the structure of LNMO to construct a new bond with Li^+. Since the bonding energy

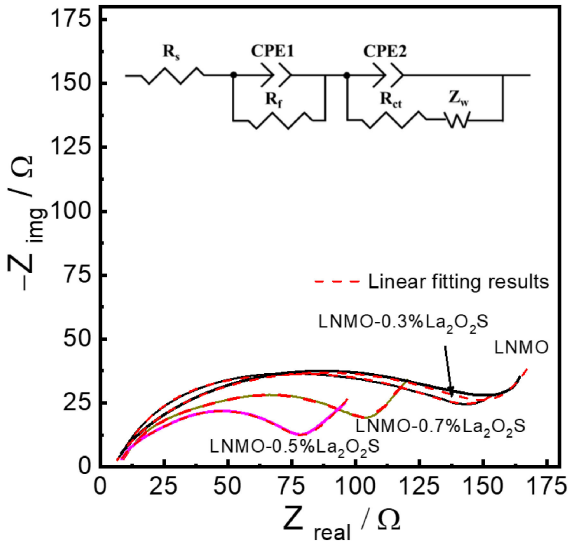

Figure 10. Nyquist plots after the 50th cycle of the charge/discharge (1 C/10 C) of LNMO-x%La_2O_2S ($x = 0$, 0.3, 0.5, and 0.7). The inset figure shows an equivalent circuit for fitting these Nyquist plots. R_s is Ohmic resistance of the electrolyte and other parts of the cell, R_f is the film resistance of the electrolyte decomposition, R_{ct} is the charge transfer resistance, CPE is the constant phase elements and Z_w is Warburg impedance controlled by the Li^+ diffusion process in a low-frequency region.

of Li-S (312.5 kJ mol^{-1}, 298 K) is smaller than that of Li-O (340.5 kJ mol^{-1}, 298 K), the Li^+ in the Li-S bond of the La_2O_2S-doped LNMO composite electrode may tend to be preferentially released during the electrochemical measurements, leaving some empty sites for the smooth migration of Li^+. This kind of effect is considered to be favorable for enhancing the kinetics process of Li^+ in the LNMO-0.5La_2O_2S composite electrode and thus give improved electrochemical performance. To analyze the Li-storage behaviors of the LNMO-x%La_2O_2S ($x = 0$, 0.3, 0.5, and 0.7) composite electrodes, electrochemical impedance spectroscopy (EIS) was performed after the measurement of rate-performance, and the Nyquist plots are shown in Fig. 10. The Nyquist plots were fitted with a conventional Randle's equivalent circuit (inset in Fig. 10)[46] by

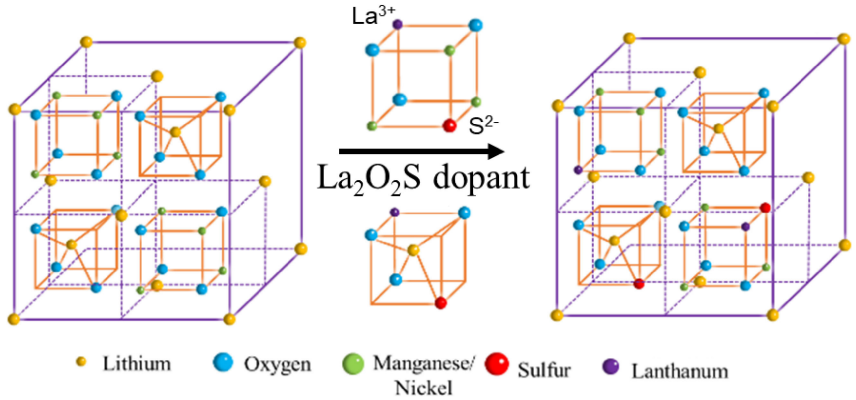

Figure 11. A schematic illustration of the La^{3+} and S^{2-} co-doped strategy using La_2O_2S as a dopant on $LiNi_{0.5}Mn_{1.5}O_4$ with spinel structure.

Table 3. Resistances evaluated by the fitting results of Nyquist plots of LNMO-x%La_2O_2S (x = 0, 0.3, 0.5, and 0.7).

Samples	R_s (Ω)	R_f (Ω)	R_{ct} (Ω)
LNMO	4.2	30.0	149.0
LNMO-0.3 %La_2O_2S	4.9	22.3	129.1
LNMO-0.5 %La_2O_2S	6.9	15.5	55.1
LNMO-0.7 %La_2O_2S	6.9	6.7	103.8

ZView software (Scribner Associates, Inc., Southern Pines, NC, USA) and the fitting results are shown in Table 3. Ohmic resistance (R_s) from the electrolyte and other parts of the cell in the Nyquist plots was estimated to be around 4–7 Ω among the different electrodes, which was attributed to the similar electrochemical environment. As for the film resistance (R_f) from the electrolyte decomposition and the charge transfer resistance (R_{ct}), a significant difference was observed after the measurements of cycling performance. According to the fitting results in Table 3, the value of R_f decreased with an increase in the ratio of La_2O_2S doping into the LNMO composite electrode. For pristine LNMO electrodes, R_f was around 30.0 Ω and for LNMO-0.7 %La_2O_2S, the value was only 6.7 Ω. Interestingly, the value of R_{ct} decreased with an increase in the ratio of La_2O_2S doping into the LNMO composite electrode. For example, for pristine LNMO electrodes, R_{ct} was 149.0 Ω and for the LNMO-0.5 %La_2O_2S composite electrode, R_{ct} was only 55.1 Ω. This trend was consistent, except that R_{ct} of the LNMO-0.7 %La_2O_2S composite electrode was around 103.8 Ω. Therefore, doping of LNMO with La_2O_2S can form a favorable interface for lithium ion to transfer between the electrolyte and electrode. However, this transfer of the lithium ion would be hindered when the ratio of the La_2O_2S dopant in the LNMO reaches a certain value due to the blocking effect of large atoms such as La and S.

4. Conclusions

In this study, a facile co-precipitation method for synthesizing the transition metal carbonate precursor assisted by solid-state annealing was applied. As a result, dual-element (La, S) co-doped LNMO materials were successfully synthesized by introducing the stable oxysulfide La_2O_2S. Additionally, the co-doped strategy in this study is further illustrated in Fig. 11. With an increase in the ratio of La_2O_2S, the cubic lattice parameter of the LNMO materials shrank slightly. Due to the higher bonding energy of the La–O bond, and the restricted reaction activity of Mn^{3+}/Mn^{4+} in the LNMO spinel structure, the structural stability of the LNMO material was optimized. The LNMO-0.5 %La_2O_2S composite electrode showed an outstanding Li^+ diffusion rate and cycling stability even under 10 C, which was attributed to the synergistic effects of La and S elements. The presence of La^{3+} in the transition metal sites can effectively stabilize the spinel crystal structure of the LNMO material. Moreover, since the bonding energy of Li–S was less than that of the Li–O from the LNMO structure, the newly formed bond of Li–S might improve the kinetics of the lithium-ion diffusion process in the crystal structure of LNMO, particularly under a high current density. Accordingly, LNMO material doped with La and S by using La_2O_2S as the dopant showed excellent Li^+ storage performance during electrochemical measurements. This strategy could be a promising approach to enhance Li^+ mobility in positive materials with poor ionic conductivity and improve rate performance for the next generation of LIBs.

CRediT Authorship Contribution Statement

Wencong Wang: Data curation (Lead), Investigation (Lead), Writing – original draft (Lead)
Hiromasa Hanzawa: Supervision (Lead)
Ken-ichi Machida: Supervision (Equal)
Kohei Miyazaki: Supervision (Equal)
Takeshi Abe: Supervision (Equal)

Data Availability Statement

The data that support the findings of this study are openly available under the terms of the designated Creative Commons License in J-STAGE Data listed in D1 of References.

Conflict of Interest

The authors declare no conflict of interest in the manuscript.

References

D1. W. Wang, H. Hanzawa, K. Machida, K. Miyazaki and T. Abe, *J-STAGE Data*, https://doi.org/10.50892/data.electrochemistry.17157863, (2021).
1. K. M. Abraham, *J. Phys. Chem. Lett.*, **6**, 830 (2015).
2. M. S. Whittingham, *Chem. Rev.*, **114**, 11414 (2014).
3. V. Etacheri, R. Marom, R. Elazari, G. Salitra, and D. Aurbach, *Energy Environ. Sci.*, **4**, 3243 (2011).
4. C. Zhu, R. E. Usiskin, Y. Yu, and J. Maier, *Science*, **358**, eaao2808 (2017).
5. R. Marom, S. F. Amalraj, N. Leifer, D. Jacob, and D. Aurbach, *J. Mater. Chem.*, **21**, 9938 (2011).
6. A. Kraytsberg and Y. Ein-Eli, *Adv. Energy Mater.*, **2**, 922 (2012).
7. L. Lu, X. Han, J. Li, J. Hua, and M. Ouyang, *J. Power Sources*, **226**, 272 (2013).
8. O. K. Park, Y. Cho, S. Lee, H.-C. Yoo, H.-K. Song, and J. Cho, *Energy Environ. Sci.*, **4**, 1621 (2011).

9. X. Zhang, F. Cheng, J. Yang, and J. Chen, *Nano Lett.*, **13**, 2822 (2013).
10. Y. K. Sun, S. T. Myung, B. C. Park, J. Prakash, I. Belharouak, and K. Amine, *Nat. Mater.*, **8**, 320 (2009).
11. R. Santhanam and B. Rambabu, *J. Power Sources*, **195**, 5442 (2010).
12. J. Cho, Y. J. Kim, and B. Park, *Chem. Mater.*, **12**, 3788 (2000).
13. A. Yamada, S. C. Chung, and K. Hinokuma, *J. Electrochem. Soc.*, **148**, A224 (2001).
14. H. Wang, T. A. Tan, P. Yang, M. O. Lai, and L. Lu, *J. Phys. Chem. C*, **115**, 6102 (2011).
15. J. Song, D. W. Shin, Y. Lu, C. D. Amos, A. Manthiram, and J. B. Goodenough, *Chem. Mater.*, **24**, 3101 (2012).
16. H. Chen, L. Lan, M. Huang, X. Liang, Y. Zhao, and F. Tang, *Int. J. Electrochem. Sci.*, **12**, 11309 (2017).
17. G. Liu, J. Zhang, X. Zhang, Y. Du, K. Zhang, G. Li, H. Yu, C. Li, Z. Li, Q. Sun, and L. Wen, *J. Alloys Compd.*, **725**, 580 (2017).
18. R. Amin and I. Belharouk, *J. Power Sources*, **348**, 311 (2017).
19. S. Nageswaran, M. Keppeler, S.-J. Kim, and M. Srinivasan, *J. Power Sources*, **346**, 89 (2017).
20. K. Lee, G. J. Yang, H. Kim, T. Kim, S. S. Lee, S.-Y. Choi, S. Choi, and Y. Kim, *J. Power Sources*, **365**, 249 (2017).
21. J. Xiao, X. Chen, P. V. Sushko, M. L. Sushko, L. Kovarik, J. Feng, Z. Deng, J. Zheng, G. L. Graff, Z. Nie, D. Choi, J. Liu, J. G. Zhang, and M. S. Whittingham, *Adv. Mater.*, **24**, 2109 (2012).
22. M.-M. Deng, B.-K. Zou, Y. Shao, Z.-F. Tang, and C.-H. Chen, *J. Solid State Electrochem.*, **21**, 1733 (2017).
23. Z. Yang, Y. Jiang, J.-H. Kim, Y. Wu, G.-L. Li, and Y.-H. Huang, *Electrochim. Acta*, **117**, 76 (2014).
24. F. Ulu Okudur, J. D'Haen, T. Vranken, D. De Sloovere, M. Verheijen, O. M. Karakulina, A. M. Abakumov, J. Hadermann, M. K. Van Bael, and A. Hardy, *RSC Adv.*, **8**, 7287 (2018).
25. G. B. Zhong, Y. Y. Wang, Z. C. Zhang, and C. H. Chen, *Electrochim. Acta*, **56**, 6554 (2011).
26. Y.-F. Deng, S.-X. Zhao, Y.-H. Xu, K. Gao, and C.-W. Nan, *Chem. Mater.*, **27**, 7734 (2015).
27. Y.-K. Sun, S. W. Oh, C. S. Yoon, H. J. Bang, and J. Prakash, *J. Power Sources*, **161**, 19 (2006).
28. J. Li, S. Li, S. Xu, S. Huang, and J. Zhu, *Nanoscale Res. Lett.*, **12**, 414 (2017).
29. R. Singhal, S. R. Das, M. S. Tomar, O. Ovideo, S. Nieto, R. E. Melgarejo, and R. S. Katiyar, *J. Power Sources*, **164**, 857 (2007).
30. S. Liu, H. Zhao, M. Tan, Y. Hu, X. Shu, M. Zhang, B. Chen, and X. Liu, *Materials*, **10**, 859 (2017).
31. M. Mo, K. S. Hui, X. Hong, J. Guo, C. Ye, A. Li, N. Hu, Z. Huang, J. Jiang, J. Liang, and H. Chen, *Appl. Surf. Sci.*, **290**, 412 (2014).
32. D. Arumugam and G. Paruthimal Kalaignan, *J. Electroanal. Chem.*, **648**, 54 (2010).
33. D. Arumugam, G. Kalaignan, and P. Manisankar, *Solid State Ionics*, **179**, 580 (2008).
34. X. Qin, J. Guo, M. Zhou, B. Zong, L. Wang, and G. Liang, *Eur. J. Inorg. Chem.*, **2018**, 1275 (2018).
35. D. Lu, L. Yuan, Z. Chen, R. Zeng, and Y. Cai, *J. Alloys Compd.*, **730**, 509 (2018).
36. M. Pokhrel, A. k. Gangadharan, and D. K. Sardar, *Mater. Lett.*, **99**, 86 (2013).
37. P. Han, L. Zhang, L. Wang, and Q. Zhang, *Rare Earths*, **29**, 849 (2011).
38. H. Sun, Y. Chen, C. Xu, D. Zhu, and L. Huang, *J. Solid State Electrochem.*, **16**, 1247 (2012).
39. D. K. Lee, S. C. Han, D. Ahn, S. P. Singh, K. S. Sohn, and M. Pyo, *ACS Appl. Mater. Interfaces*, **4**, 6842 (2012).
40. P. Gao, L. Wang, L. Chen, X. Jiang, J. Pinto, and G. Yang, *Electrochim. Acta*, **100**, 125 (2013).
41. T.-F. Yi and Y.-R. Zhu, *Electrochim. Acta*, **53**, 3120 (2008).
42. Y. Luo, T. Lu, Y. Zhang, L. Yan, S. S. Mao, and J. Xie, *J. Alloys Compd.*, **703**, 289 (2017).
43. X. H. Rui, N. Ding, J. Liu, C. Li, and C. H. Chen, *Electrochim. Acta*, **55**, 2384 (2010).
44. H. Sun, X. Kond, B. Wang, T. Luo, and G. Liu, *Int. J. Electrochem. Sci.*, **12**, 8609 (2017).
45. W. Liu, Q. Shi, Q. Qu, T. Gao, G. Zhu, J. Shao, and H. Zheng, *J. Mater. Chem. A*, **5**, 145 (2017).
46. W. Wang, H. Liang, L. Zhang, S. V. Savilov, J. Ni, and L. Li, *Nano Res.*, **10**, 229 (2017).